Materials Characterization 217 (2024) 114360

Contents lists available at ScienceDirect

Materials Characterization

journal homepage: www.elsevier.com/locate/matchar

Microstructure characteristics for improved thermal shock reliability of sintered Ag—Al paste in SiC power module

Fupeng Huo [a], Chuantong Chen [a,*], Zheng Zhang [a], Yicheng Zhang [a], Aiji Suetake [a], Kazutaka Takeshita [b], Yoshiji Yamaguchi [b], Yashima Momose [b], Katsuaki Suganuma [a]

[a] Flexible 3D System Integration Laboratory, The Institute of Science and Industrial Research, Osaka University, Osaka, Japan
[b] Yamato Scientific Co. Ltd., Tokyo, Japan

ARTICLE INFO

Keywords:
Sintering
Sustained release effect
Interface
Thermal shock
TEM

ABSTRACT

To meet the harsh thermal shock (−50–250 °C) requirements of power device packaging, a novel sintered Ag-based die attach material based on the sustained release effect of Al was proposed. In this study, Al particles with natural core-shell structure covered with Al_2O_3 layer were selected as the ideal doping-phase, and micron Al particles doped sintered Ag composite paste (AgAl) was prepared. First, the microstructural evolution of sintered AgAl joints during thermal shock was studied. The results showed that Al particles effectively suppressed the cracks generation, which attributed to the sustained release effect of Al element. To clarify sustained release mechanism of Al, the interfaces evolution between Ag and Al particles was investigated. In the initial stage, Al was covered by the Al_2O_3 layer, preventing inter-diffusion between Ag and Al. As the thermal shock proceeds, the Al_2O_3 film was fractured, achieving direct contact between metal Al and Ag. Diffusion thus takes place. For the sintered Ag5Al joint, the shear strength was 17.3 MPa after 1000 cycles, which is 1.57 times that of pure sintered Ag joint. These results indicate the successful development of low-cost, high-reliability die attachment materials for use in harsh thermal shock environments.

1. Introduction

Wide bandgap (WBG) semiconductor SiC has garnered significant attention due to its outstanding performance characteristics, including high electron mobility, high breakdown voltage, high operation temperature, and low switching losses [1–3]. It exhibits immense potential for applications in electric vehicles, aerospace, smart grids, and other domains [4–6]. To fully leverage the performance advantages of SiC, SiC power modules need to operate at higher temperatures, reaching up to 250 °C [7]. In this context, significant challenges are posed to the packaging of power modules, particularly concerning the die attach layer. Traditional die attach materials, such as Sn-based solder alloys, no longer suffice to meet the requirements of WBG modules. To address this issue, various alternative methods have been proposed, including transient liquid phase bonding, high-temperature solders, and sintered Ag [8–10]. Among these methods, sintered Ag is regarded as one of the most promising alternatives due to its excellent heat resistance and electrical conductivity [11].

However, for an ideal die attach material to be applied in SiC power modules, it is imperative to possess not only excellent heat resistance but also excellent reliability. Among numerous reliability concerns [12–14], thermal shock is regarded as one of the most prevalent factors leading to power device failure, especially under harsh thermal shock conditions within the range of −50 to 250 °C. This necessitates that die attach materials not only endure high temperatures of up to 250 °C but also withstand the alternating loads resulting from temperature differentials of up to 300 °C. Current sintered Ag materials have been primarily proposed to fulfill high-temperature service requirements. They suffice for most high-temperature storage conditions due to Ag's inherently high melting point and excellent thermal conductivity [15,16]. Nevertheless, the reliability of sintered Ag under thermal shock conditions is notably unsatisfactory. Liu et al. [17] prepared sintered Ag/DBA joint at 250 °C for 30 min without pressure, when subjected to 1000 thermal shock cycles, the microstructure deteriorated significantly and the substrate also cracked, resulting in a decrease in strength from 37.6 to about 5.0 MPa, representing a 86.7 % decline compared to the initial state. Xu et al. [18] utilized modified DBC substrates to mitigate thermal stresses, and prepared sintered Ag joint at 250 °C for 60 min under pressure of 5

* Corresponding author.
E-mail address: chenchuantong@sanken.osaka-u.ac.jp (C. Chen).

https://doi.org/10.1016/j.matchar.2024.114360
Received 9 June 2024; Received in revised form 3 September 2024; Accepted 9 September 2024
Available online 10 September 2024

MPa. The problems of microstructure degradation and delamination were still severe. The corresponded shear strength also decreased from 81.9 MPa to 8.2 MPa after 1000 cycles at the range of −50-250 °C. This can be attributed to poor strength and ductility of sintered Ag [19]. Inadequate strength prevents it from withstanding the stresses resulting from coefficient of thermal expansion (CTE) mismatches, while limited ductility fails to effectively absorb the strains induced by alternating loads, ultimately leading to crack formation. Unfortunately, until now, there have been scarcely any reports of die attach materials specifically designed for the harsh thermal shock conditions encountered in SiC power modules. To address this challenge, a novel sintered Ag-based die attach material tailored for harsh thermal shock conditions in SiC power modules should be developed.

To enhance material performance, two methods, microalloying and composite materials, are commonly employed [20,21]. In most cases, both approaches prove effective in improving material properties. However, for die attach materials exposed to prolonged thermal shock conditions, the improvement strategy should align with the material's long-term service requirements. Microalloying involves the intentional introduction of solute atoms into a base metal through inter-diffusion, leading to solid solution formation, precipitation of phases, as well as brittle intermetallic compounds (IMCs) [22]. In the case of sintered Ag, if a highly diffusing metal element is introduced initially, it may lead to the formation of brittle IMCs, detrimental to material's ductility. Thus, microalloying is not a suitable in the initial stages of thermal shock. On the other hand, the composite materials approach refers that incorporates second-phase particles that do not react with the Ag matrix, inhibiting grain boundary migration and preventing coarsening of sintered Ag [23]. However, composite materials face challenges in long-term thermal shock cycling conditions due to the absence of atomic diffusion between the matrix and second-phase particles, making them less capable of withstanding the alternating loads imposed during harsh thermal shock. Therefore, the ideal choice is a combination of the two strategies. In the initial stage, composite materials are used to establish effective bonding between the second phase and the Ag matrix without generating IMCs, as there is no diffusion. In the following demanding thermal shock stage, the interdiffusion of atoms between the second phase particles and the Ag matrix needs to be implemented to achieve a robust interface bond and enhance the properties of the Ag matrix.

To implement the above design requirements, the added phase should belong to metal. However, in the initial stages, a ceramic shell structure is needed to prevent their reaction with the Ag matrix, forming IMCs. Moreover, during thermal shock cycling, this shell needs to be gradually opened to enable microalloying with Ag matrix. Thus, an ideal reinforcing phase comprises a core-shell structure consisting of a metallic core and a ceramic shell. Traditional methods for preparing core-shell materials primarily involve selective corrosion, soft template method, and double solvent method [24,25]. However, most of these methods are complex, costly, and challenging to apply industrially. In contrast to artificially synthesized core-shell materials with intricate processes, micro-sized Al particles have attracted our interest. Micro-sized Al particles exhibit a natural core-shell structure, with a metallic Al core and an Al_2O_3 ceramic shell on the surface [26]. Due to the differences in CTE between metallic Al and Al_2O_3, as well as the inherent brittleness of the Al_2O_3 ceramic layer, the Al_2O_3 ceramic shell gradually fractures during thermal shock cycling, opening the “gateway” for Ag and Al diffusion, making microalloying possible. Additionally, Huo et al. [27] prepared an ideal AgAl solid solution, resulting in an 83.0 % increase in strength and a 40.0 % increase in ductility compared to pure Ag. This demonstrates that the solid solution of Al in Ag can simultaneously enhance its strength and ductility. Furthermore, the cost-effectiveness of Al further reduces the cost of sintered Ag materials. In summary, micro-sized Al aligns perfectly with the aforementioned design requirements. On the other hand, effective bonding between the Ag matrix and the Al_2O_3 layer is crucial for achieving outstanding performance in sintered AgAl composite pastes.

In this study, a sintered Ag-based die attach materials applied to harsh thermal shock conditions were specially designed based on the sustained release principle. Micron-sized Al particles, coated with Al_2O_3 layer, were chosen as the second phase to prepare sintered AgAl composite paste. Subsequently, sintered AgAl/DBC (direct bonded copper) joints were fabricated, and the microstructure evolution and mechanical performance of the joints were investigated with various harsh thermal shock cycles. In particular, the interfacial evolution of Ag and Al particles was systematically studied using transmission electron microscopy (TEM) during harsh thermal shock. These findings are expected to provide theoretical insights and experimental foundations for the development of die attachment materials used in harsh thermal shock conditions.

2. Materials and methods

2.1. Materials

The micron-sized Ag flake was jointly developed by our Lab. and Fukuda Metal Foil and Power Ltd., Kyoto, Japan. SEM images of the Ag sample are shown in Fig. 1(a), displaying a flake-like morphology with lateral dimensions ranging from 0.9 to 5.8 μm and an average size of 1.8 μm. In the thickness view, the size ranges from 0.3 to 0.5 μm. Fig. 1(c) presents a TEM image of the Ag flake, revealing the presence of numerous nanocrystals within the flake. Statistical analysis indicates that the nanocrystals have a size ranging from 32.8 to 145.6 nm, with an average size of 61.3 nm. This suggests that micron-sized flakes contain many nanocrystals, setting them apart from other sintered Ag materials. Fig. 1(d) shows the magnified view of area 1 in Fig. 1(c), where many.

numerous high-density dislocations and sub-grain boundary can be observed, indicating that the Ag flake is in a high-energy state. These unique characteristics can be attributed to the specific ball-milling process employed for Ag flake production. The Al particles were provided by the Institute for Materials Research, Saitama, Japan. SEM images of the Al particles are displayed in Fig. 1(b), showcasing spherical, ellipsoidal, and short columnar shapes, with sizes ranging from 0.7 to 19.8 μm and an average size of 3.0 μm. The organic solvent CELTOL-IA was supplied by Daicel Corporation, Kyoto, Japan.

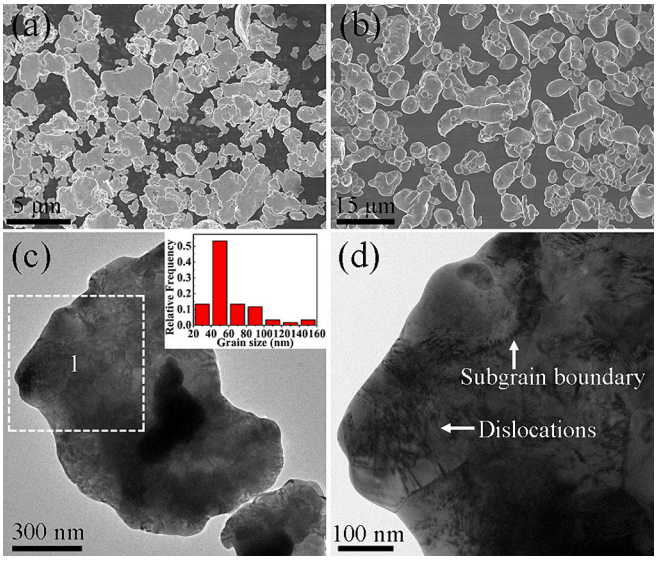

Fig. 1. Morphology of Ag flake and Al particles. SEM image of (a) Ag flake, (b) Al particles. TEM image of (c) Ag flake, (d) magnified view of area 1.

2.2. Preparation of sintered AgAl series composite paste and bonding process

The Ag flakes and Al particles with varying mass fractions (0, 2 wt%, 5 wt%) were mixed in an alcohol solution. They were stirred at a rotational speed of 100 r/min for 1 h using magnetic stirring to ensure uniform mixing of Ag flakes and Al particles. Subsequently, the mixture was dried at 50 °C for 24 h to evaporate the alcohol. Afterward, the mixed powder was combined with the organic solvent CELTOL-IA (10 wt%) using a mixing device (ARV-310, THINKY, Japan) at 2000 r/min for 5 min to fabricate the sintered AgAl composite paste.

In the bonding program, SiC with dimensions of 3 mm × 3 mm was used as a dummy die. Their backs were sputter-coated with Ti (100 nm) and Ag (1 μm), respectively. The substrate employed was a newly developed DBC substrate, with surfaces coated with electroplate Ni (10 μm), electroless Ni (0.5 μm), electroless Pt (0.1 μm), and electroless Ag (1 μm), respectively, as illustrated in Fig. 2(a). Initially, the sintered pure Ag and AgAl composite paste were printed onto the DBC substrate. Subsequently, the SiC die was mounted onto the paste, as shown in Fig. 2 (b). The samples were then heated to 250 °C with the rate of 10 °C/min in ambient air, held for 1 h, and finally cooled to room temperature. During the sintering process, the pressure of 1 MPa was applied. The same sintering process was used for the three pastes (Ag, Ag2Al, and Ag5Al). Finally, the bonded samples underwent thermal shock cycling in the temperature range of −50 °C to 250 °C for 100, 500, and 1000 cycles, respectively. The dwell time at maximum (250 °C) and minimum (−50 °C) temperatures were set to 30 min, respectively.

2.3. Characterization and testing

The sintered AgAl joints, both at the initial stage and after harsh thermal shock cycling, underwent crack detection using x-ray computed tomography (CT). The CT was operated at a voltage and current of 90 kV and 100 μA, respectively. The cross-sectional microstructure of the sintered AgAl joints was observed using scanning electron microscopy (SEM, SU8020, Hitachi, Japan). The evolution of the interface between Ag and Al particles in the sintered layer was investigated using TEM (JEM-ARM200F, JEOL, Japan). TEM samples were prepared using focused ion beam (FIB, FB-2100, Hitachi, Japan). The mechanical properties of the sintered joints were determined through shear tests (ERS-400, Nordon DAGE, UK), with shear strength being the average of six samples. The shear fracture surfaces were examined using SEM. The thermal conductivity of the sintered AgAl composite pastes was measured using the laser flash method (LFA 467 Hyperflash, Netzsch). Thermal conductivity samples of the composite pastes (Ag, Ag2Al, and Ag5Al) were prepared using the same sintering process as described in section 2.2. The final samples were machined into cylindrical shapes with a diameter of 10 mm and a height of 2 mm. The electrical resistivity of the sintered AgAl composite pastes was measured using the four-point probe method (MCP T610, Loresta-GP, Mitsubishi Chemical). Resistivity samples of the composite pastes (Ag, Ag2Al, and Ag5Al) were also prepared following the same sintering process outlined in section 2.2. The final dimensions of the resistivity samples were 35 mm × 10 mm × 0.1 mm (length × width × height).

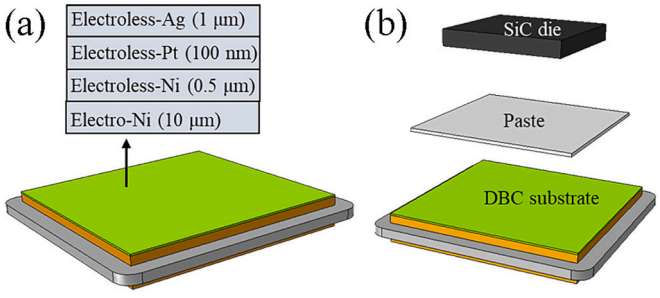

Fig. 2. The schematic diagram of (a) new developed DBC substrate, (b) bonding program.

In addition, in-situ TEM was also performed. Electron beam irradiation was used as a heat source to observe the nanoparticle ejection phenomenon of micron Ag flakes. During the irradiation process, photos were taken every 2 min. The voltage and current during the operation were 200 kV and 60.3 μA, respectively.

3. Results and discussion

3.1. Properties of sintered AgAl composite pastes

3.1.1. Mechanical properties of sintered AgAl joints during harsh thermal shock cycles

Fig. 3 illustrates the mechanical properties evolution of sintered AgAl joints under different thermal shock cycles. Overall, for all samples, the shear strength gradually decreases as the cycles increase (shown in Fig. 3(a)). However, compared to sintered pure Ag joints, sintered AgAl joints exhibit a slower rate of decline in shear strength (shown in Fig. 3(b)). Furthermore, as the Al content increases, the degree of shear strength reduction decreases gradually, indicating that the addition of Al can effectively inhibit the degradation of joint performance.

In the initial stage, the shear strength of sintered Ag was 70.5 MPa, demonstrating good sintering performance for micron-sized flake Ag paste. The addition of Al moderately reduced the shear strength, the shear strengths for sintered Ag2Al and Ag5Al joints were 46.8 and 42.1 MPa, respectively. This is because Al particles covered with Al_2O_3 layers initially act as obstacles, impeding the connection between sintering necks and thereby inhibiting the sintering process of Ag flakes. When reached 100 cycles, we observed a more pronounced decrease in shear strength for sintered Ag joints compared to sintered AgAl joints. The shear strength of sintered Ag joints decreased to 44.3 MPa, a 37.2 % decrease compared to the initial stage. In contrast, sintered Ag2Al and Ag5Al joints show reductions of 25.4 % - 28.5 % compared to the initial stage, which is lower than sintered Ag joints.

When the number of cycles reached 500, the shear strength of sintered Ag further decreased to 19.7 MPa, while the shear strengths of sintered Ag2Al and Ag5Al were 17.8 MPa and 20.6 MPa, respectively. The result of Ag5Al is already higher than sintered Ag. When the number of thermal shock cycles reached 1000, the shear strength of sintered Ag decreased to 11.0 MPa, which is a significant 84.4 % reduction compared to the initial value. While the shear strengths of sintered Ag2Al and Ag5Al after 1000 cycles were 13.3 and 17.3 MPa, respectively, representing reductions of 71.6 % and 58.9 % compared to the initial stage. These values are lower than that of the sintered Ag joint. This indicates that the AgAl composite paste exhibits better thermal shock performance reliability compared to pure Ag paste. Furthermore, with an increasing amount of Al added, the degree of decline gradually decreases, suggesting that the addition of Al particles significantly improves the thermal shock reliability. For the sintered Ag5Al joint, the shear strength was 17.3 MPa after 1000 cycles, which was above the die shear standard (MIL-STD-883 K, 7.8 MPa) [28]. Additionally, this shear strength of sintered of Ag5Al joint also higher than traditional Pb5Sn under similar harsh service conditions [29]. Moreover, the cost of micron-sized Ag5Al is significantly lower than that of nano-sintered Ag. These results indicate the successful development of low-cost, high-reliability die attachment materials for use in harsh thermal shock environments.

3.1.2. Thermal conductivity and electrical resistivity of sintered AgAl pastes

Fig. 4(a) shows the thermal conductivity of the sintered AgAl composite pastes with various Al additions. The thermal conductivity of the sintered pure Ag was measured at 164.2 W/(m·K). With the addition of Al particles, a decreasing trend in thermal conductivity was observed.

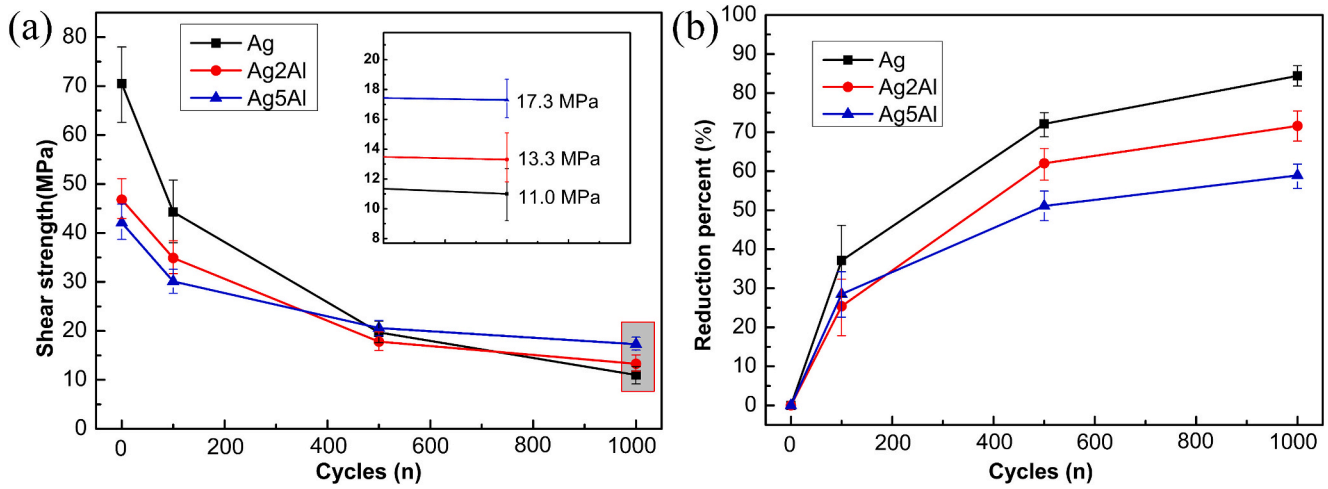

Fig. 3. Mechanical properties evolution of sintered AgAl joints under different thermal shock cycles. (a) The shear strength. (b) Reduction percent.

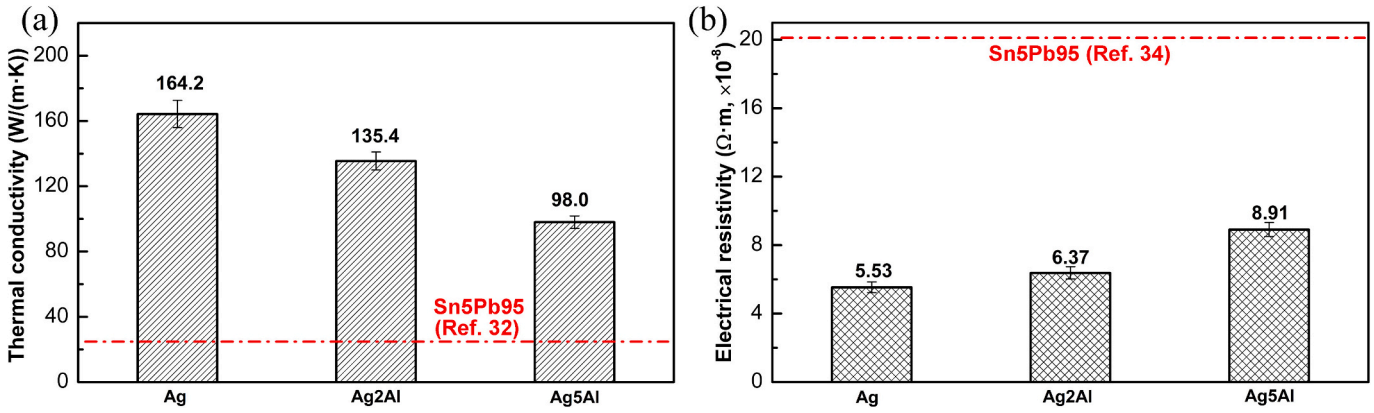

Fig. 4. Thermal conductivity and electrical resistivity of sintered pure Ag and Ag Al composite pastes. (a) Thermal conductivity, (b) electrical resistivity.

The thermal conductivity of sintered Ag2Al and Ag5Al were measured at 135.4 W/m·K and 98.0 W/m·K, respectively. This reduction in thermal conductivity attributed to two main factors: Firstly, Al has a lower thermal conductivity than Ag [30]. Secondly, as the Al content increases, the interfacial area between Ag and Al particles increases, weakening the electron-phonon coupling effect in interfacial heat transfer, leading to higher thermal resistance [31]. Nevertheless, the result of Ag5Al is still higher than that of traditional Sn5Pb95 solder [32].

Fig. 4(b) shows the electrical resistivity of the sintered AgAl composite pastes. The electrical resistivity of sintered pure Ag was measured at 5.53×10^{-8} Ω·m, and it increased gradually with the addition of Al particles. The results of sintered Ag2Al and Ag5Al were measured at 6.37×10^{-8} Ω·m and 8.91×10^{-8} Ω·m, respectively. For pure metals (where impurities and defects can be ignored), electrical resistivity mainly arises from electron scattering caused by lattice vibrations [33]. The addition of Al particles disrupts the electron scattering in pure Ag, resulting in an increase in resistivity. The electrical resistivity of Ag5Al was measured at 8.91×10^{-8} Ω·m, which is still lower than that of traditional Sn5Pb95 solder [34].

In summary, the addition of Al particles slightly reduces the thermal conductivity of pure Ag and increases its electrical resistivity. However, the thermal and electrical properties of the AgAl composite paste are still superior to those of traditional Sn5Pb95 solder. In conclusion, combining the results of sections 3.1.1 and 3.1.2, the sintered AgAl composite pastes exhibit good mechanical-thermal-electrical comprehensive performance, as well as high-reliability under harsh thermal shock conditions.

3.2. *Microstructure evolution of various Al doped sintered ag joints during harsh thermal shock*

During the harsh thermal shock process, due to the difference in the inherent properties of the substrate, die attachment materials, and SiC die that make up the joint, such as CTE and plasticity [35]. This leads to the generation of numerous cracks during thermal shock, affecting the reliability of the joint. To make full view of crack in sintered Ag joints during different thermal cycling processes, X-ray CT was conducted. Fig. 5 shows the CT results for sintered AgAl joints at different thermal shock cycles. In the initial stage (Fig. 5(a)), no cracks were observed, indicating good sintering performance of the micron-sized Ag flake. When the thermal shock increased to 1000 cycles, the overall view (Fig. 5(b)) displayed visible cracks. The high-magnification view of area 1 is shown in Fig. 5(c), where the white mesh-like patterns represent longitudinal cracks within the sintered Ag layer. Statistical results indicated that the average distance between these cracks at this stage was 33.4 μm. A comparison between Figs. 5(a) and (b) reveals a significant degradation in the microstructure of sintered Ag after 1000 cycles of harsh thermal shock, which could reduce the reliability of power devices. Figs. 5(d) and (e) show the CT images of the Ag2Al joint in its initial stage and after 1000 cycles, respectively. The high-magnification view of area 2 in Fig. 5(e) is presented in Fig. 5(f). The crack density was lower than that of the pure Ag joint, with a corresponding crack spacing of 60.2 μm. When the Al content reached 5 wt%,

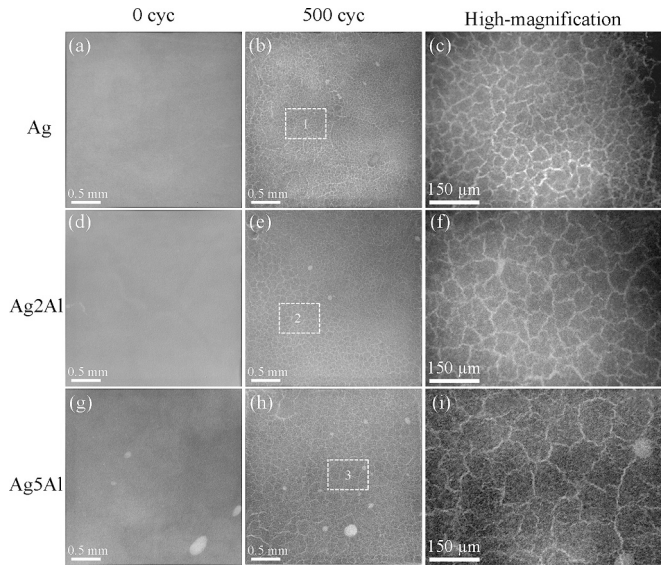

Fig. 5. CT results for sintered AgAl joints during thermal shock cycles. (a), (b) Ag, (c) high-magnification of area 1. (d), (e) Ag2Al, (f) high-magnification of area 2. (g), (h) Ag5Al, (i) high-magnification of area 3.

as shown in Figs. 5(g), (h), and (i), the crack density was further reduced, with a crack spacing of 90.2 μm. These results demonstrated that the addition of Al particles can effectively suppress crack formation during long-term thermal shock cycling.

According to the above results, since the Ag5Al joint showed higher strength and fewer cracks, the following analysis will focus on Ag and Ag5Al joints.

Fig. 6(a) illustrates the SEM image of pure sintered Ag joint at the initial stage. The joint consists of three parts: the SiC die, sintered Ag layer, and metallized DBC substrate. In the initial stage, the SiC die was well bonded to the substrate via pure sintered Ag. The sintered Ag layer exhibited a uniform porous structure, and the sintered Ag layer and SiC die showed a continuous flat interface. Similarly, there was a good interface between the sintered Ag and the DBC substrate, and no deformation of the substrate was observed in the initial stage. However, when the thermal shock cycle reached 500 cycles (Fig. 6(b)), the sintered Ag layer significantly coarsened, and numerous penetrating cracks were observed. Furthermore, due to stress migration of Ag atoms [36,37], the contact area between the sintered Ag layer and the substrate gradually decreased. Under the accumulation of thermal stress, transverse cracks occurred at the interface between the sintered Ag layer and the DBC substrate. These transverse cracks gradually extended and merged, ultimately forming localized delamination. The high-magnification of area 1 and 2 in Fig. 6 (b) are shown in Fig. 6(b1) and (b2), respectively. Due to the formation of longitudinal cracks, the coarsened sintered Ag structure seemed re-"cut" into a porous-like structure (marked with dotted curves in Fig. 6(b1)), which actually represents localized coarsened sintered Ag fractured due to the formation of many cracks. Correspondingly, at the interface (Fig. 6(b2)), the stress-induced migration of Ag atoms gradually weakened the interface, eventually resulting in delamination.

When the thermal shock cycle reached 1000 cycles (Fig. 6(c)), the microstructure further coarsened, with only a few isolate pores observable, as most of the sintered pores had merged into longitudinal cracks. Compared to 500 cycles, the density of penetrating longitudinal cracks increased further. Statistical results indicated a spacing of 33.0 μm between longitudinal cracks, consistent with the X-ray CT result in Fig. 5(c). Similarly, transverse delamination was also observed at the interface between the sintered Ag layer and the DBC substrate. The high-magnification of area 3 and 4 in Fig. 6 (c) are shown in Fig. 6(c1) and (c2), respectively. The sintered Ag layer underwent structural coarsening due to thermal effects, forming almost Ag blocks; At the same time, these Ag blocks were separated again due to crack formation. The region marked with dotted curves in Fig. 6(c1) represents the sintered Ag divided by cracks, as the contours on both sides fit well. This ultimately led to a fragmentation trend in the sintered porous Ag structure. Correspondingly, the effective bonding area at the interface further decreased.

In summary, the microstructure of pure Ag sintered joints significantly degraded after experiencing harsh thermal shock, including penetrating cracks in the longitudinal direction and localized delamination in the transverse direction. This would reduce the reliability of the joint and significantly increase the thermal resistance of the power module, ultimately accelerating the failure of the power module [38,39].

Fig. 7(a) shows the SEM image of sintered Ag5Al joint at the initial stage. The SiC die and DBC substrate exhibited good bonding with the sintered Ag5Al composite paste. In the die attachment layer, Al particles were uniformly dispersed within the sintered Ag matrix, and no agglomeration was observed. This was attributed to the effective preparation process of the composite material. Additionally, flat interfaces were formed between the sintered Ag—Al layer and both the SiC die and the DBC substrate. When the thermal shock cycle reached 500 cycles (Fig. 7(b)), the sintered Ag5Al layer exhibited microstructural coarsening and cracks, mainly non-penetrating cracks. Importantly, there was no observed delamination at the interface between the sintered Ag5Al layer and the DBC substrate. This indicated that the addition of Al could effectively suppress Ag atom stress migration, improving microstructural stability. The high-magnification of area 1 and 2 in Fig. 7 (b) are shown in Fig. 7(b1) and (b2), respectively. Fig. 7(b1) shows the microstructure of the area where there is almost no longitudinal crack re-segmented between two adjacent longitudinal cracks after 500 cycles. Furthermore, at the interface region (Fig. 7(b2)), there was a good bond

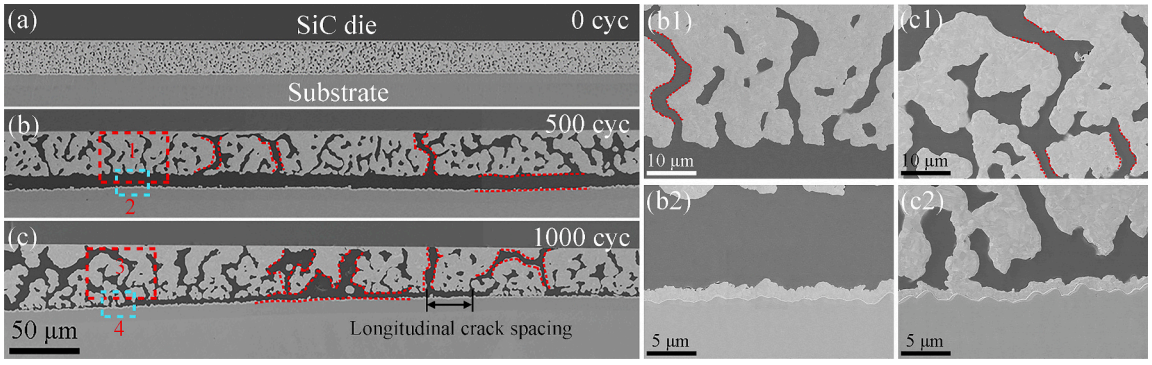

Fig. 6. SEM images of sintered Ag joint during thermal shock. (a) 0 cycle. (b) 500 cycles. (c) 1000 cycles. High-magnification of (b1) area 1 and (b2) area 2 in Fig. 6 (b). High-magnification of (c1) area 3 and (c2) area 4 in Fig. 6 (c).

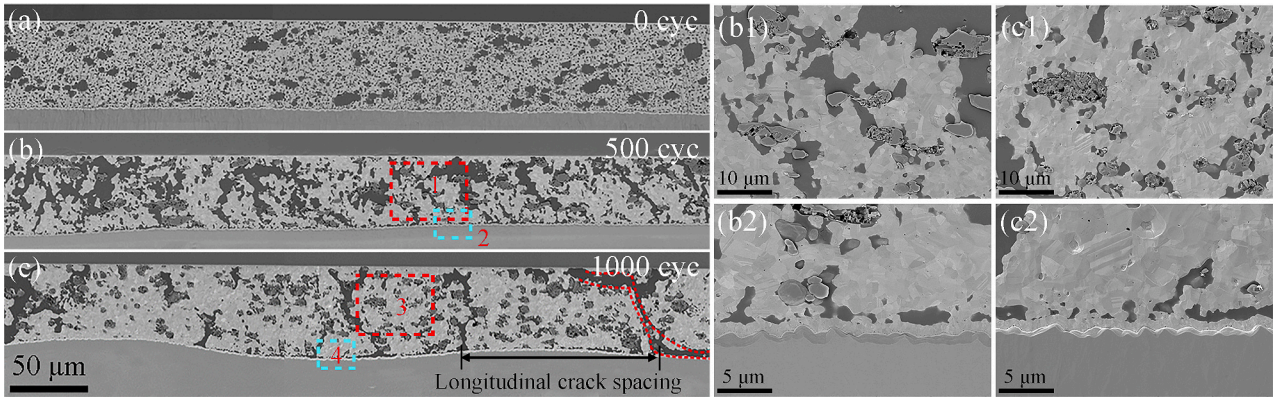

Fig. 7. SEM images of sintered Ag5Al joint during thermal shock. (a) 0 cycle. (b) 500 cycles. (c) 1000 cycles. High-magnification of (b1) area 1 and (b2) area 2 in Fig. 7 (b). High-magnification of (c1) area 3 and (c2) area 4 in Fig. 7 (c).

between the sintered layer and the DBC substrate.

When reached 1000 cycles (Fig. 7(c)), the cracks mainly consisted of longitudinal cracks and a few delamination. The average spacing between longitudinal cracks was 90.5 μm, which was consistent with the CT results in Fig. 5(c1). Due to prolonged thermal shock, transverse cracks appeared in the upside and bottom interface areas. As transverse and longitudinal cracks extended, they eventually formed tortuous cracks (marked with dotted curves). However, compared to Fig. 6(c), the degree of delamination was suppressed. The high-magnification of area 3 and 4 in Fig. 7 (c) are shown in Fig. 7(c1) and (c2), respectively. As seen in Fig. 7(c1), the sintered Ag further coarsened, almost forming a bulk structure. The Al particles were embedded tightly within the Ag matrix in localized regions. The fragmentation phenomenon in the sintered layer disappeared. It could improve the strength of the sintered layer. At the interface region, there was a good bond between the sintered layer and the DBC substrate. The effective bonding area at the interface was nearly unchanged compared to the 500-cycle stage. Additionally, there was no apparent stress migration phenomenon of Ag, exhibiting the good stability of the interface.

In summary, the above results indicate that under long-terms harsh thermal shock loading, the addition of Al particles effectively suppressed the generation of both longitudinal and transverse cracks. In addition, an interesting phenomenon was observed in sintered Ag5Al layer. The relevant results are shown in Fig. 8. Fig. 8(a) shows the Ag/Al interface in sintered layer at the initial stage, where Al particles tightly bonded with the sintered Ag, and the Al particles were in bulk state at this stage. When reached 500 cycles (Fig. 8(c)), Al particles formed numerous regularly arranged rectangular voids, and the number of rectangles in the edge area was more than that in the middle area. This structure was not observed in the initial stage. With increasing cycles, the previously solid bulk portion also transformed into a porous structure. Thus, after 1000 cycles of thermal shock (Fig. 8(c)), the solid Al particles became uniform porous structure composed of rectangular pores, indicating a gradual release of Al atoms during the thermal shock process. This phenomenon was first reported in the field of power device packaging. However, the question remains: where did these Al atoms go, and how were they released? These questions require further investigation.

In general, a natural Al_2O_3 film forms on the surface of Al particles, which acts as a barrier hindering the diffusion of Al atoms with external atoms [40,41]. However, during severe thermal shock processes, significant deformation occurred in the die attach layer due to the alternating loads generated by the differing CTE of the components in the sintered joint. Under the action of this alternating load, what changes will happen to the Al_2O_3 on the surface of Al particles is worth our in-depth discussion, which will be discussed in detail later.

3.3. Fracture analysis

Fig. 9 depicts the fracture surfaces of sintered AgAl joints at different thermal shock cycles. Figs. 9(a)-(c) represent the fracture surfaces of sintered Ag at different cycles. Overall, during the entire thermal shock process, fracture occurs at the interface between the sintered layer and the DBC substrate, but it exhibits varying surface morphologies. In the initial stage (Fig. 9(a)), many dimples can be observed, indicating significant plastic deformation near the interface during the shear process, demonstrating good bonding strength. When the cycles reached 500 (Fig. 9(b)), The roughness of the fracture surface significantly reduced. This was because during the thermal shock process, localized delamination has occurred between the sintered layer and the DBC substrate. Consequently, only a few fractured sintered necks can be observed, resulting in a smoother fracture surface. Fig. 9(c) shows the fracture surface after 1000 cycles, the fracture surface appeared flat, with almost no torn sintered necks observed. After prolonged harsh thermal shock, the region of delamination between the sintered layer and the substrate further increased, and longitudinal cracks were also multiplied. Both factors worsen the interface, making it easier for fractures to occur in the interface region during shear test.

However, new phenomenon was observed for sintered Ag5Al joint.

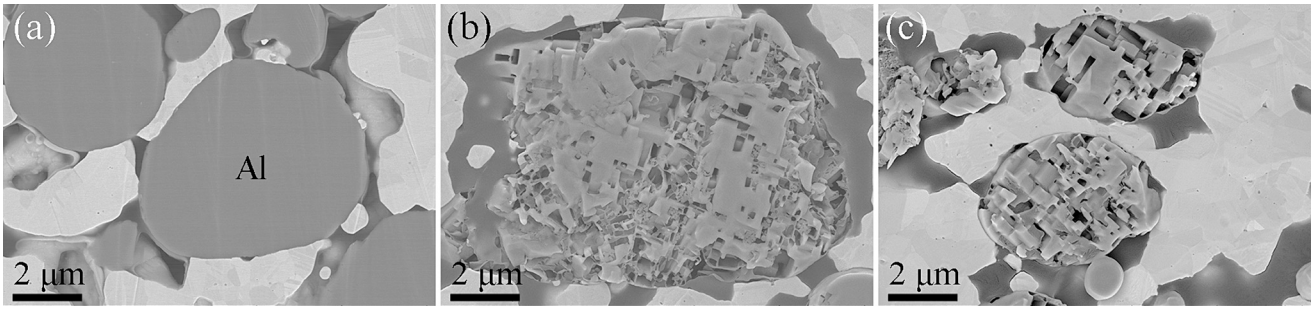

Fig. 8. Solid to porous state transformation of Al particles during thermal shock cycling. (a) 0 cycle. (b) 500 cycles. (c) 1000 cycles.

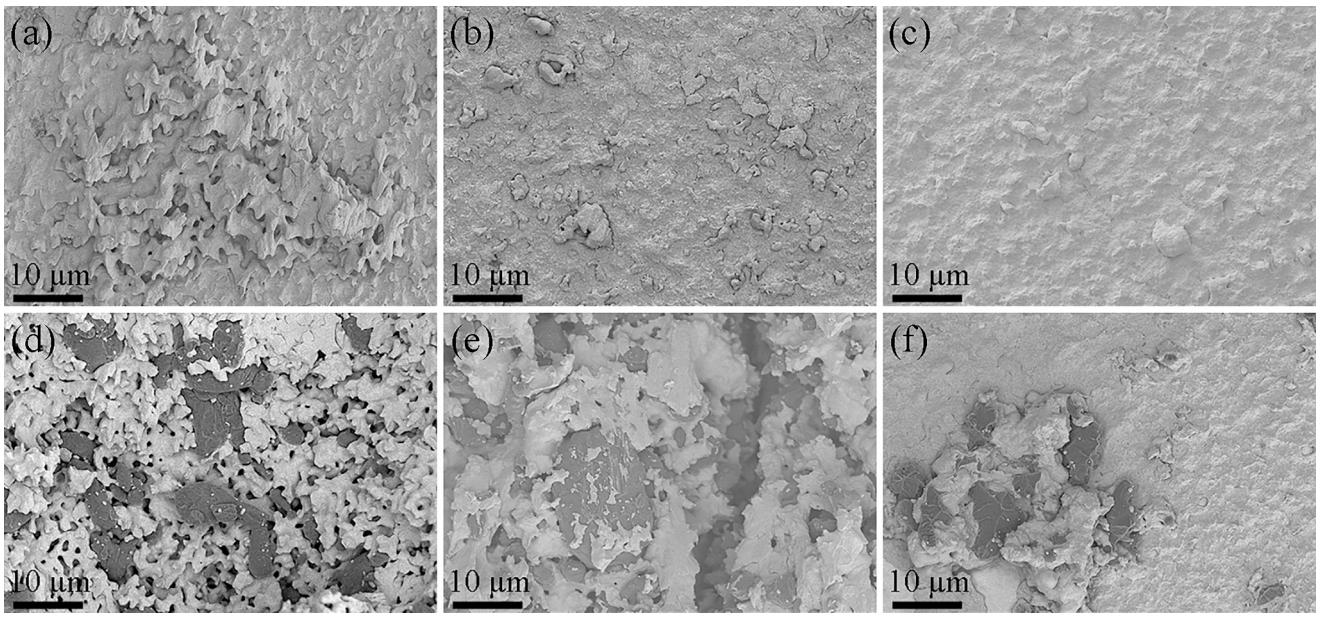

Fig. 9. Fracture surfaces of sintered AgAl joints at different thermal shock cycles. Sintered Ag joint at (a) 0, (b) 500, and (c) 1000 cycles, respectively. Sintered Ag5Al joint at (d) 0, (e) 500, and (f) 1000 cycles, respectively.

For the sintered Ag5Al joints (Figs. 9(d)-(f)), fracture initially occurred within the sintered Ag5Al layer. This is attributed to the influence of Al addition, which affects the sintering process, resulting in a weakening of the sintered layer's strength. In Fig. 9(d), the dark phase represented Al particles, where Al particles embedded within the Ag matrix. Even after shear fracture, residual Ag was still visible on the Al particle surfaces, indicating a strong bond at the Ag—Al interface. As the number of thermal shock cycles increased, fractures continue to take place within

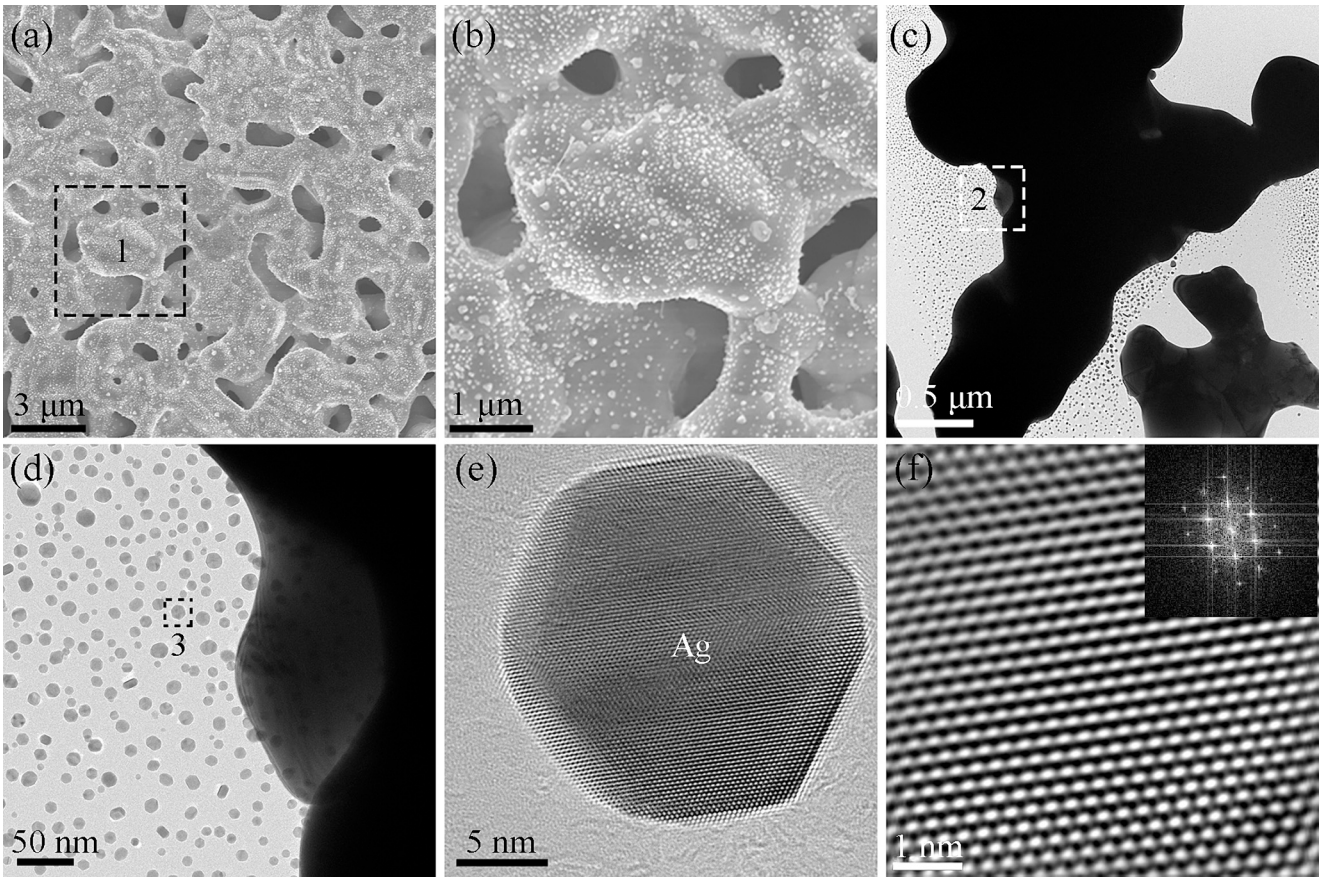

Fig. 10. Ag nanoparticle precipitation phenomenon from micron Ag flake. (a) SEM image of surface morphology of the Ag paste after sintering. (b) The magnified view of area 1 in Fig. 10(a). (c) TEM image of micron Ag flake after electron beam irradiation. (d) The magnified view of area 2 in Fig. 10(c). (d) HRTEM image of area 3 in Fig. 10(e). (f) fast Fourier transformation (IFFT) image of Fig. 10(e).

the sintered layer until 500 cycles. When the number of thermal shock cycles reached 1000 (Fig. 9(f)), a change in fracture path occurred, Part of the fracture occurred in the sintering layer, while part of the fracture in the interface region between the sintered Ag5Al and the DBC substrate. This change was attributed to the delamination in the interface region, as previously mentioned in Fig. 7(c).

In summary, for sintered Ag joints, fractures always occur in the interface region between the sintered layer and the DBC substrate during the entire thermal shock process. With the addition of Al particles, the fracture path gradually shifts toward the sintered layer. Fractures within the sintered layer primarily involve the rupture of sintered Ag necks and the rupture at the interface between sintered Ag and Al particles.

3.4. Sustained release mechanism of Al particles in the sinter Ag5Al layer during harsh thermal shock

To address the questions raised by SEM observations, where Al goes and how it is released, a more in-depth investigation of the interfaces between Ag and Al particles is required using TEM. Additionally, for composite materials, regulating the interface is crucial for achieving optimal performance. Therefore, in this section, we systematically analyze the interfaces between Ag and Al particles in the sintered Ag15Al layer at the initial stage and after 1000 cycles of thermal shock.

Before conducting the interface analysis, one point needs to be clarified. The natural Al_2O_3 thin film on the surface of Al particles makes bonding between Al and Ag challenging in air. However, according to Fig. 8(a), and Figs. 9(d) and (e), the sintered Ag and Al particles bond well, attributed to the use of the specific Ag flake.

Fig. 10(a) shows the surface morphology of the Ag paste after sintering. The magnified view of area 1 in Fig. 10(a) is shown in Fig. 10(b). It can be seen that numerous nanoparticles precipitated on the surface of the sintered Ag. Additionally, when the Ag flake was placed in a TEM chamber and heated with electron beam energy, numerous ultrafine Ag nanoparticles appeared around the micro-scale Ag flake, as identified in Figs. 10(e)-(f). These precipitated Ag nanoparticles not only facilitate rapid self-sintering but can also modify the surface of the doped Al particles.

Fig. 11 presents the in-situ TEM images of the Ag flake under electron beam irradiation. The dotted circle in Fig. 11(a) indicates the area irradiated by the electron beam. In the initial stage (Fig. 11(a)), no nanoparticles were observed. When the irradiation time reached 2 min (Fig. 11(b)), some particles of 2 nm size were observed. With increased irradiation time, more particles were ejected from the micro-scale Ag flake. Simultaneously, the ejected ultrafine nanoparticles began to coalesce and grow. When the irradiation time reached 14 min (Fig. 11 (h)), the contour of the Ag flake had changed significantly compared to the initial stage. The missing portions had transformed into ultrafine nanoparticles. This special phenomenon is used to achieve effective bonding between Ag and Al. The previous research has verified it [42]. Next, we will systematically analyze the sustained release mechanism of Al particles during thermal shock.

3.4.1. Ag/Al interface at initial stage

Fig. 12 presents TEM, HRTEM and EDS images of the Ag/Al interface in the sintered Ag5Al layer in the initial stage. Fig. 12(a) displays the TEM image of the Ag/Al interface, and the EDS line analysis along line a-a 1 in Fig. 12(a) is shown in Fig. 12(f). Combining Figs. 12(a) and 11(f), it can be discerned that the dark area on the left side represents Ag, while the light gray area on the right side represents Al. Between them, there is a continuous thin bright layer. In this thin region, EDS indicates a higher percentage of oxygen (marked with a dotted circle), suggesting the presence of oxides. To further investigate the bonding interface, HRTEM was conducted. Fig. 12(b) shows high magnification view of area 1 in Fig. 12(a). In Fig. 12(b), a distinct interface is visible, with a bright region in the middle with the thickness of approximately 9 nm. The fast Fourier transformation (FFT) image of area 2 is shown in Fig. 12(c),

displaying well-defined diffraction spots that can be indexed as (111), $(1\bar{1}1)$, and (200) planes of Ag along the $[02\bar{2}]$ axis. The corresponding inverse FFT (IFFT) image in Fig. 12(c1) revealed periodic lattice fringes with an interplanar spacing of 0.236 nm, representing $(1\bar{1}1)$ plane of Ag. These results confirmed that area 2 in Fig. 12(b) was to Ag. Similarly, the FFT image of area 3 in Fig. 12(b) is presented in Fig. 12(d), where no diffraction spots are observed. Instead, an amorphous ring appeared, and the corresponding IFFT image indicated an unordered atomic state. Combined with the EDS results in Fig. 12(f) and reported research [43], this suggests that Area 3 corresponded to

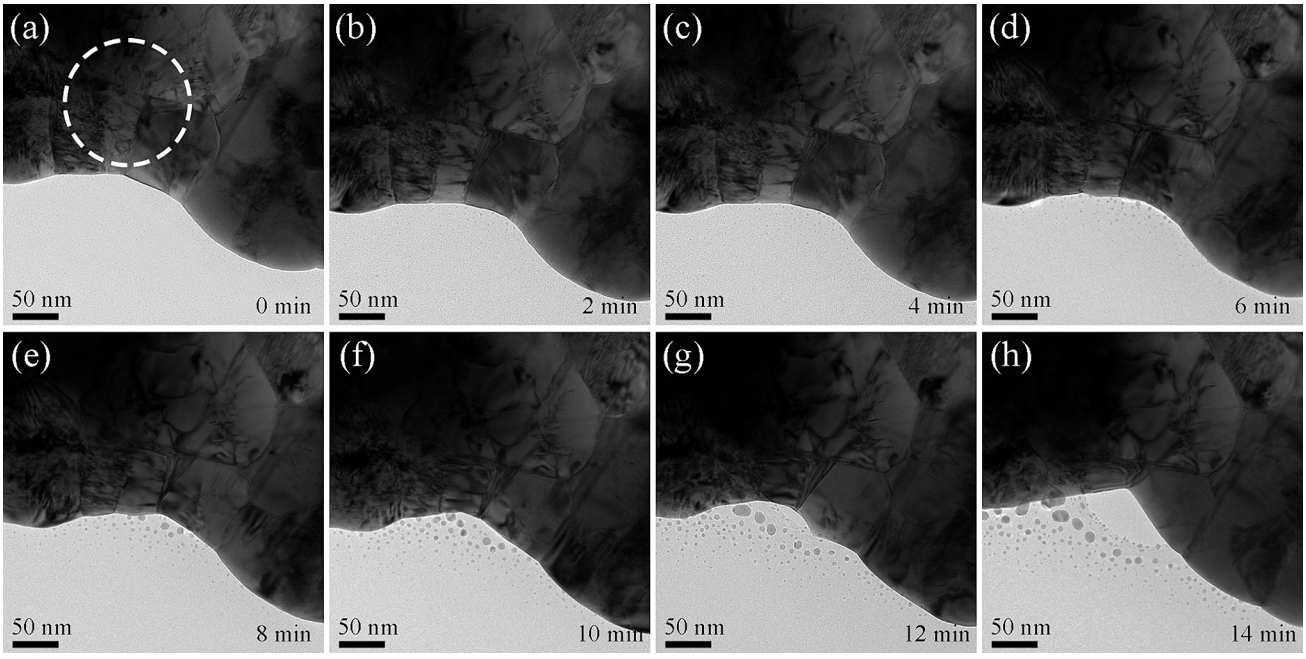

Fig. 11. The in-situ TEM images of the Ag flake under electron beam irradiation. (a) 0 min, (b) 2 min, (c) 4 min, (c) 6 min. (a) 8 min, (b) 10 min, (c) 12 min, (c) 14 min.

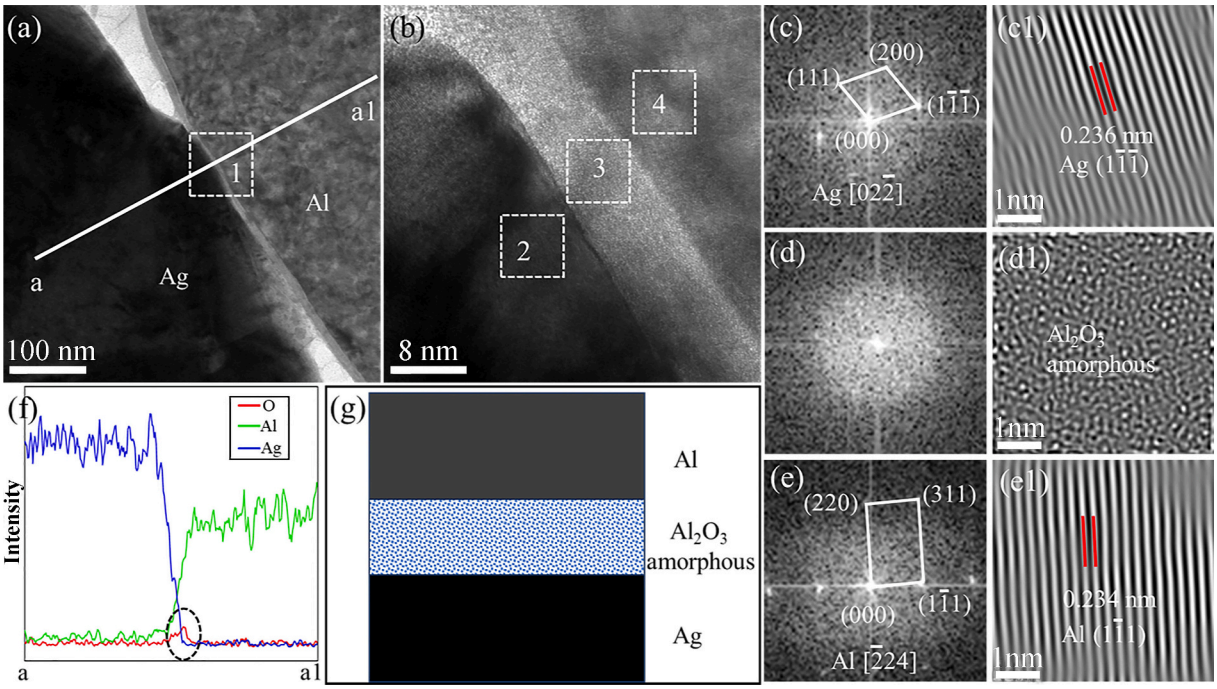

Fig. 12. TEM, HRTEM and EDS images of the Ag/Al interface in the sintered Ag5Al layer in the initial stage. (a) TEM image, (b)HRTEM image of area1 in Fig. 12(a). (c) FFT and (c1) IFFT image of area 2 in Fig. 12(b). (d) FFT and (d1) IFFT image of area 3 in Fig. 12(b). (e) FFT and (e1) IFFT image of area 4 in Fig. 12(b). (f) EDS of a-a1 line in Fig. 12(a). (g) Schematic diagram of the Ag and Al particle interface in initial stage.

amorphous Al_2O_3. The FFT image of area 4 is shown in Fig. 12(e), also displaying well-defined diffraction spots that can be indexed as Ag's (220), (1$\bar{1}$1), and (311) planes, with the crystallographic axis as [$\bar{2}$24]. The corresponding IFFT image in Fig. 12(e1) reveals periodic lattice fringes with an interplanar spacing of 0.234 nm, representing (1$\bar{1}$1) plane of Ag. These results confirmed that area 4 in Fig. 12(b)

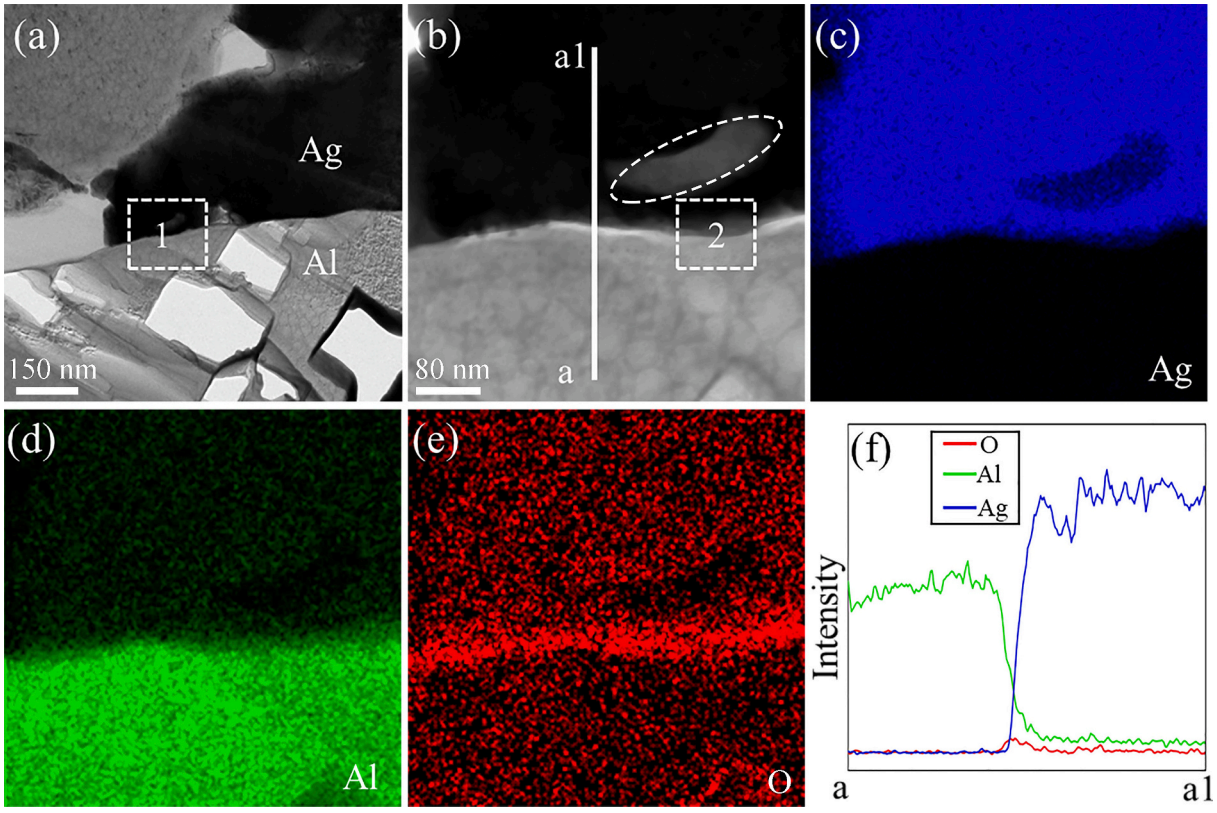

Fig. 13. TEM and EDS results of the Ag/Al interface in the sintered Ag5Al layer after 1000 cycles. (a) TEM image. (b) enlarged view of area 1 in Fig. 13(a). EDS maps of (c) Ag, (d) Al, and (c) O, respectively. (f) EDS line analysis along a-a1 in Fig. 13(b).

corresponded to Al. Area 3 represented a naturally occurring oxide layer on the surface of Al particles. Combining Figs. 12(a), (b), and (f), it could be concluded that Al_2O_3 acted as a continuous barrier layer among Ag and Al, inhibiting the mutual diffusion of Ag and Al. During sintering, the bonding between Ag and Al was essentially a direct bonding between sintered Ag and the Al_2O_3 film. The schematic diagram of the Ag and Al particle interface in initial stage was shown in Fig. 12(g), where metallic Al was covered by the Al_2O_3 layer, and sintered Ag bonded with the Al_2O_3 layer, preventing mutual diffusion between Ag and Al.

3.4.2. *Ag/Al interface after 1000 thermal shock cycles*

Fig. 13 presents the TEM and EDS results of the Ag/Al interface in the sintered Ag5Al layer after 1000 cycles. In Fig. 13(a), the interface between sintered Ag and Al is depicted. Where the light-colored regions in the upper left corner and at the bottom represent Al, while the central region corresponds to sintered Ag. Sintered Ag exhibited good bonding with Al particles after 1000 cycles. In the Al region at the bottom, rectangular gaps can be observed, consistent with SEM observations. Fig. 13(b) shows an enlarged view of area 1 in Fig. 13(a). as can be seen, Ag was located at the.

upper side, and Al was at the lower side. Within the interface region, there are intermittent bright areas, which differ.

from the continuous bright layer seen in Fig. 12(a). Additionally, a light elongated structure was observed in the Ag region further away from the interface (marked with a dotted circle). EDS maps, shown in Fig. 13(c)-(e), provided further insight. EDS results indicated that this elongated structure was a void formed in sintered Ag due to thickness contrast. Fig. 13(d) displayed Al elemental maps, revealing an interesting phenomenon. Aside from detecting Al elements in the region where Al particles are present, some Al elements were also detected in the upper Ag region. This suggested that some Al elements have diffused into the Ag through the interface layer. The EDS line analysis along a-a 1 in Fig. 13(b) is presented in Fig. 13(f), where the red, green, and blue lines represent O, Al, and Ag elements, respectively. The green line in the Ag region exhibits higher intensity than the background and the red line, indicating the presence of Al elements in Ag region.

Until now, we can address the first question raised at the beginning of section 3.4: where did the Al go? The result shows that Al diffused into the sintered Ag region.

However, as noted in Fig. 12, in the initial stages, the surface of Al was enveloped by a layer of naturally occurring Al_2O_3. After undergoing thermal shocks, how did it manage to penetrate this oxide layer and diffuse into the sintered Ag? To clarify this issue, HRTEM was conducted in the interface region. Fig. 14(a) represented HRTEM images of area 2 in Fig. 13(b). The upper dark region corresponds to Ag, the lower region to Al, and the central interface layer exhibits varying contrasts, which are divided by a red dotted curve. On the left side, an unordered atomic distribution was observed, akin to the state found in area 3 of Fig. 12(b). On the right side, some lattice fringes were discernible. To gain insight into these observations, the DigitalMicrograph software was employed to conduct FFT and IFFT. The FFT result for area 1 in Fig. 14(a) is shown in Fig. 14(b), and it could be identified as (200), ($\bar{1}$11), and (111) planes of Al, with a axis of [0$\bar{2}$2]. Corresponding IFFT images are depicted in Fig. 14(b1). Similarly, the FFT result for area 2 in Fig. 14(a) is presented

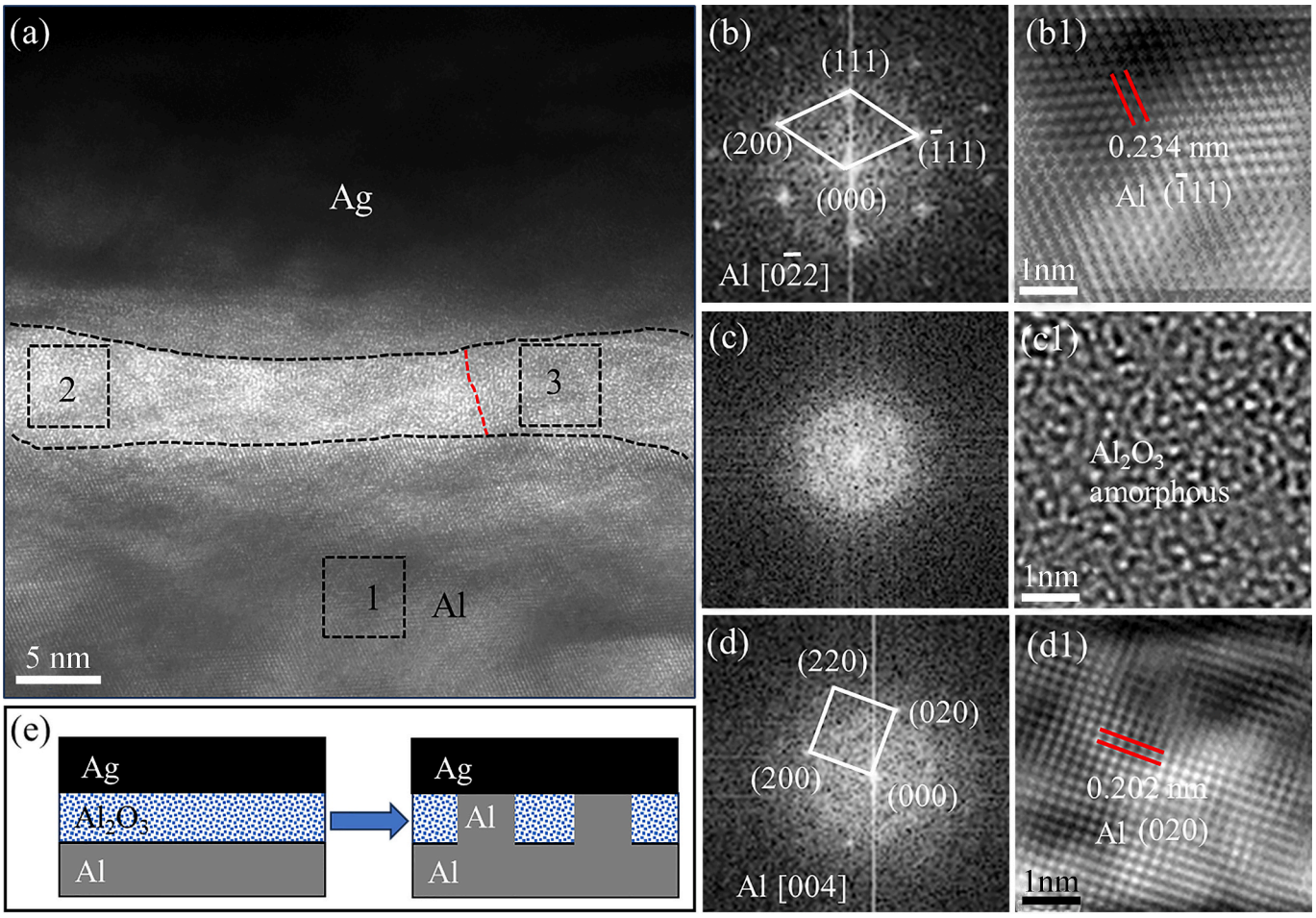

Fig. 14. HRTEM image of the Ag/Al interface in the sintered Ag5Al layer after 1000 cycles. (a) Magnified view of area 2 in Fig. 13(b). (b) FFT and (b1) IFFT image of area 1 in Fig. 14(a). (c) FFT and (c1) IFFT image of area 2 in Fig. 14(a). (d) FFT and (d1) IFFT image of area 3 in Fig. 14(a). (e) Schematic diagram of the Ag and Al particle interface evolution after 1000 cycles.

in Fig. 14(c), revealing an amorphous ring, with the corresponding IFFT image (Fig. 14(e1)) showing a disordered atomic state. This suggests that this region belongs to Al_2O_3 amorphous, consistent with the interface structure in initial stage. However, on the right side of the red line, different results emerged. The FFT result for area 3 is shown in Fig. 14 (d), and it can be identified as (200), (020), and (220) planes of Al along the [004] axis. Corresponding IFFT images are presented in Fig. 14(d1). This indicates the presence of metallic Al in the interface layer, facilitating direct contact between Al and Ag, consequently resulting in the diffusion of Al into Ag. This represents a change from the situation observed in the initial stages.

During the harsh thermal shock loading range of −50 to 250 °C, substantial stresses and strains were generated within the DBC substrate, sintered layer, and SiC die due to differences in CTE. Moreover, thermal mismatches also occurred within the sintered layer itself, owing to the distinct CTEs of Ag, Al, and Al_2O_3 layer. Among them, Al_2O_3 exhibited a weaker resistance to strain due to its inherent brittleness, leading to the fracture of the Al_2O_3 layer under harsh thermal shock conditions. This fracture provided pathways for the diffusion of Al atoms. As thermal shock continued, Al particles with the locally breached Al_2O_3 layer underwent plastic deformation, with deformed metallic Al filling the fractured areas of Al_2O_3. This facilitated direct contact between metallic Al and Ag. For area 1 and area 3 in Fig. 14(a), although both composed of Al, they exhibited different orientations due to plastic deformation [44,45]. Thus, the bridge for Ag and Al diffusion was established. Once metallic Al and Ag were in directly contact, diffusion was facilitated due to the similarities in their crystal structures (both belonging to fcc) and lattice constants [46,47]. Diffusion can easily occur under temperature loads. This also explained why the diffusion of Al element into Ag is detected in Fig. 13. As the diffusion proceeded, more and more Al atoms were diffused into the Ag, resulting in a reduction of Al atoms within the Al particles, and finally many pores were formed with Al particles, as shown in Fig. 8.

The schematic diagram of the interface evolution between Ag and Al particles after 1000 thermal shock cycles is shown in Fig. 14(e). In the initial stage, Al was covered by the Al_2O_3 layer, the sintered Ag was bonded to the Al_2O_3 layer, and no interdiffusion occurred between Ag and Al. As the thermal shock cycles increased, the Al_2O_3 film on the surface of the Al particles was broken; the plastic deformation of the Al particles caused by thermal shock filled the broken area, achieving direct contact between metal Al and Ag. Diffusion of Al thus took place. As the number of thermal shock cycles continue increases, the diffusion channels gradually opened and further diffusion occurred. This also answered the second question: how Al atoms were released into Ag.

In summary, the sustained release mechanism of Al in sintered Ag5Al layer during thermal shock is as follows. In the initial stage, the bonding of Ag and Al_2O_3 on the surface of Al particles was realized through the jetting phenomenon of ultra-fine Ag nanoparticles of Ag flake. As the thermal shock proceeds, the Al_2O_3 film was deformed and fractured, and the gate of Ag and Al diffusion was opened, thereby realizing the diffusion between Al and Ag. This unique phenomenon was referred to as the “sustained release effect of Al elements” during harsh thermal shock processes. The schematic diagram is shown in Fig. 15.

For a heterogeneous interface subjected to prolonged severe thermal shock conditions, such as the Ag/Al interface, if no barrier layer (Al_2O_3) initially exists, direct bonding of metallic Ag to metallic Al would lead to the formation of brittle IMCs, like Ag_2Al and Ag_3Al. This would deteriorate the interface and diminish the performance of the composite material. However, if the barrier layer persists throughout the service life, it would hinder the diffusion between Ag and Al. Non-diffusive bonding would inevitably result in poor reliability during harsh thermal shock. In this study, design strategy changes from passive to active, ingeniously capitalizing on the Al particles' inherent Al_2O_3 film and the external load of severe thermal shock. During thermal shock cycling, gradual “shell-breaking” (Al_2O_3 shell) allowed Al elements to be released slowly, enabling Ag and Al diffusion. When these Al atoms solid dissolved into the Ag matrix, they could exert a pinning effect on Ag grains [48,49], inhibiting the coarsening of sintered Ag during service, which also explains why the addition of Al improved the microstructure stability. In addition, the atoms in solid solution can also produce solid solution strengthening. Similarly, Huo et al. [27] prepared an ideal AgAl solid solution, resulting in an 83.0 % increase in strength and a 40.0 % increase in ductility compared to pure Ag. This demonstrates that the solid solution of Al in Ag can simultaneously enhance its strength and ductility. This also explains why cracks were significantly reduced in sintered Ag5Al layer compared to pure Ag after 1000 thermal shock cycles.

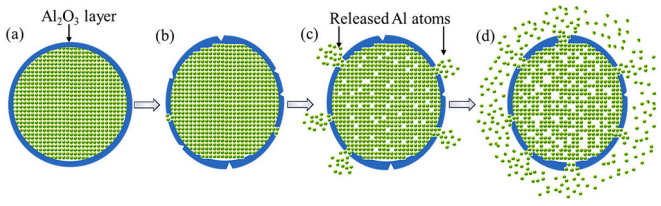

Fig. 15. Schematic illustration of sustained release mechanism of Al elements during thermal shock. (a) Initial stage; (b) Deformation and crack of Al_2O_3 layer; (c)Al atoms were released; (d) Interdiffusion was occurred.

4. Conclusions

1. The sintered AgAl composite pastes based on the sustained release effect applied to the harsh thermal shock conditions of SiC power devices was proposed. The addition of Al particles can effectively suppress crack formation during long-term thermal shock cycling, enhancing the reliability of power devices.
2. The microstructure of pure Ag sintered joints significantly degraded after experiencing severe thermal shock. The addition of Al particles effectively suppressed the generation of both longitudinal and transverse cracks, which attributed to the sustained release effect of Al. And bulk Al particle also transformed into a porous structure after long terms thermal shock. This phenomenon was first reported in the field of power device packaging.
3. The interfaces evolution between Ag and Al particles in the sintered Ag5Al layer was systematically investigated during thermal shock. In the initial stage, metallic Al was covered by the Al_2O_3 layer, and sintered Ag bonded with the Al_2O_3 layer through the jetting phenomenon of ultra-small Ag nanoparticles of Ag flake, preventing mutual diffusion between Ag and Al. As the thermal shock proceeds, the Al_2O_3 film was fractured, and the gate of Ag and Al diffusion was opened, the plastic deformation of the Al particles caused by thermal shock fills the broken area, achieving direct contact between metal Al and Ag. Diffusion thus takes place. This unique phenomenon was referred to as the “sustained release effect of Al elements” during harsh thermal shock.
4. Sintered AgAl joint exhibits better thermal shock reliability compared to pure sintered Ag joint. For the sintered Ag5Al joint, the shear strength was 17.3 MPa after 1000 cycles, which is 1.57 times that of pure sintered Ag joint. The result is better than that of traditional Pb5Sn solder. These results indicate the successful development of low-cost, high-reliability die attachment materials for use in harsh thermal shock environments.

CRediT authorship contribution statement

Fupeng Huo: Writing – original draft, Methodology, Investigation, Conceptualization. **Chuantong Chen:** Writing – review & editing, Supervision, Funding acquisition, Conceptualization. **Yicheng Zhang:** Data curation. **Aiji Suetake:** Investigation. **Kazutaka Takeshita:** Funding acquisition. **Yoshiji Yamaguchi:** Funding acquisition. **Yashima Momose:** Funding acquisition. **Katsuaki Suganuma:** Project

administration.

Declaration of competing interest

The authors declare that they have no known competing financial interests or personal relationships that could have appeared to influence the work reported in this paper.

Data availability

Data will be made available on request.

Acknowledgements

This work was supported by a project (JPNP20004) commissioned by the New Energy and Industrial Technology Development Organization (NEDO) and JSPS KAKENHI Grant Number JP22K04243, and by a research grant from The Murata Science Foundation.

References

[1] L. Wang, W. Wang, R.J.E. Hueting, G. Rietveld, J.A. Ferreira, Review of topside interconnections for wide bandgap power semiconductor packaging, IEEE Trans. Power Electron. 38 (2023) 472–490, https://doi.org/10.1109/TPEL.2022.3200469.

[2] C. Yang, Y. Pei, L. Wang, L. Yu, F. Zhang, B. Ferreira, Overvoltage and oscillation suppression circuit with switching losses optimization and clamping energy feedback for SiC MOSFET, IEEE Trans. Power Electron. 36 (2021) 14207–14219, https://doi.org/10.1109/TPEL.2021.3090031.

[3] L. Han, L. Liang, Y. Kang, Y. Qiu, A review of SiC IGBT: models, fabrications, characteristics, and applications, IEEE Trans. Power Electron. 36 (2021) 2080–2093, https://doi.org/10.1109/TPEL.2020.3005940.

[4] Z. Zeng, X. Zhang, F. Blaabjerg, H. Chen, T. Sun, Stepwise design methodology and heterogeneous integration routine of air-cooled SiC inverter for electric vehicle, IEEE Trans. Power Electron. 35 (2020) 3973–3988, https://doi.org/10.1109/TPEL.2019.2937135.

[5] Y. Gao, J. Jiu, C. Chen, K. Suganuma, R. Sun, Z.Q. Liu, Oxidation-enhanced bonding strength of Cu sinter joints during thermal storage test, J. Mater. Sci. Technol. 115 (2022) 251–255, https://doi.org/10.1016/j.jmst.2021.10.047.

[6] Z. Zhang, C. Chen, A. Suetake, M.C. Hsieh, A. Iwaki, K. Suganuma, Pressureless and low-temperature sinter-joining on bare Si, SiC and GaN by a Ag flake paste, Scr. Mater. 198 (2021) 113833, https://doi.org/10.1016/j.scriptamat.2021.113833.

[7] N. Murayama, K. Hirao, M. Sando, T. Tsuchiya, H. Yamaguchi, High-temperature electro-ceramics and their application to SiC power modules, Ceram. Int. 44 (2018) 3523–3530, https://doi.org/10.1016/j.ceramint.2017.11.140.

[8] H. Pan, J. Huang, H. Ji, M. Li, Enhancing the solid/liquid interfacial metallurgical reaction of Sn+cu composite solder by ultrasonic-assisted chip attachment, J. Alloys Compd. 784 (2019) 603–610, https://doi.org/10.1016/j.jallcom.2019.01.090.

[9] J. Xie, S. Lu, Y. Du, W. Hu, Y. Mao, Microstructural evolution and orientation-correlated origin of the coarsening behaviors in Au–Sn eutectic alloys, J. Alloys Compd. 806 (2019) 1285–1291, https://doi.org/10.1016/j.jallcom.2019.07.337.

[10] C. Chen, S. Nagao, K. Suganuma, J. Jiu, T. Sugahara, H. Zhang, T. Iwashige, K. Sugiura, K. Tsuruta, Macroscale and microscale fracture toughness of microporous sintered Ag for applications in power electronic devices, Acta Mater. 129 (2017) 41–51, https://doi.org/10.1016/j.actamat.2017.02.065.

[11] Y. Xie, Y. Wang, Y. Mei, H. Xie, K. Zhang, S. Feng, K.S. Siow, X. Li, G.Q. Lu, Rapid sintering of nano-ag paste at low current to bond large area (>100 mm2) power chips for electronics packaging, J. Mater. Process. Technol. 255 (2018) 644–649, https://doi.org/10.1016/j.jmatprotec.2018.01.017.

[12] A. Sghuri, Y. Billaud, L. Signor, D. Saury, X. Milhet, Experimental investigation of thermal conductivity during aging of nanoporous sintered silver, Acta Mater. 257 (2023) 119109, https://doi.org/10.1016/j.actamat.2023.119109.

[13] C. Chen, Z. Zhang, D. Kim, T. Sasamura, Y. Oda, M.C. Hsieh, A. Iwaki, A. Suetake, K. Suganuma, Interface reaction and evolution of micron-sized ag particles paste joining on electroless Ni-/Pd-/au-finished DBA and DBC substrates during extreme thermal shock test, J. Alloys Compd. 862 (2021) 158596, https://doi.org/10.1016/j.jallcom.2021.158596.

[14] J. Dai, J. Li, P. Agyakwa, M. Corfield, C.M. Johnson, Comparative thermal and structural characterization of sintered nano-silver and high-lead solder die attachments during power cycling, IEEE Trans. Device Mater. Reliab. 18 (2018) 256–265, https://doi.org/10.1109/TDMR.2018.2825386.

[15] Y. Tan, X. Li, G. Chen, Q. Gao, G.Q. Lu, X. Chen, Effects of thermal aging on long-term reliability and failure modes of nano-silver sintered lap-shear joint, Int. J. Adhes. Adhes. 97 (2020) 102488, https://doi.org/10.1016/j.ijadhadh.2019.102488.

[16] C. Chen, C. Choe, D. Kim, Z. Zhang, X. Long, Z. Zhou, F. Wu, K. Suganuma, Effect of oxygen on microstructural coarsening behaviors and mechanical properties of Ag sinter paste during high-temperature storage from macro to micro, J. Alloys Compd. 834 (2020) 155173, https://doi.org/10.1016/j.jallcom.2020.155173.

[17] Y. Liu, C. Chen, D. Kim, Z. Zhang, X. Long, K. Suganuma, Modified Ni/Pd/au-finished DBA substrate for deformation-resistant Ag–Au joint during long-term thermal shock test, J. Mater. Sci. Mater. Electron. 32 (2021) 20384–20393, https://doi.org/10.1007/s10854-021-06549-3.

[18] Y. Xu, X. Qiu, W. Li, S. Wang, N. Ma, M. Ueshima, C. Chen, K. Suganuma, Development of high thermal conductivity of Ag/diamond composite sintering paste and its thermal shock reliability evaluation in SiC power modules, J. Mater. Res. Technol. 26 (2023) 1079–1093, https://doi.org/10.1016/j.jmrt.2023.07.254.

[19] C. Chen, C. Choe, D. Kim, K. Suganuma, Lifetime prediction of a SiC power module by micron/submicron Ag sinter joining based on fatigue, creep and thermal properties from room temperature to high temperature, J. Electron. Mater. 50 (2021) 687–698, https://doi.org/10.1007/s11664-020-08410-5.

[20] B. Zhang, L. Xu, K. Xiong, J. He, X. Rong, Y. Mao, X. Tang, Controlling diffusion in gold bonding materials for high reliability via microalloying of trace rare earth metals, Scr. Mater. 230 (2023) 115395, https://doi.org/10.1016/j.scriptamat.2023.115395.

[21] Y.S. Jhong, H.T. Tseng, S.J. Lin, Diamond/Ag-Ti composites with high thermal conductivity and excellent thermal cycling performance fabricated by pressureless sintering, J. Alloys Compd. 801 (2019) 589–595, https://doi.org/10.1016/j.jallcom.2019.06.167.

[22] F.R. Wang, S. Guo, Y.Q. Wang, S.B. Zhu, G.M. Xie, Effect of Nb interlayer on microstructure and property of Ti-6Al-4V/690 MPa grade steel clad plate by vacuum rolling, Mater. Sci. Eng. A 882 (2023) 145450, https://doi.org/10.1016/j.msea.2023.145450.

[23] W. Jiang, J. Zhu, G. Li, F. Guan, Y. Yu, Z. Fan, Enhanced mechanical properties of 6082 aluminum alloy via SiC addition combined with squeeze casting, J. Mater. Sci. Technol. 88 (2021) 119–131, https://doi.org/10.1016/j.jmst.2021.01.077.

[24] F. Shi, J. Peng, F. Li, N. Qian, H. Shan, P. Tao, C. Song, W. Shang, T. Deng, H. Zhang, J. Wu, Design of highly durable core−shell catalysts by controlling shell distribution guided by in-situ corrosion study, Adv. Mater. 33 (2021) 1–9, https://doi.org/10.1002/adma.202101511.

[25] Z. Zhuang, W. Wang, Y. Wei, T. Li, M. Ma, Y. Ma, Preparation of polyaniline nanorods/manganese dioxide nanoflowers core/shell nanostructure and investigation of electrochemical performances, Adv. Compos. Hybrid Mater. 4 (2021) 938–945, https://doi.org/10.1007/s42114-021-00225-0.

[26] D. Mao, J. Chen, L. Ren, K. Zhang, M.M.F. Yuen, X. Zeng, R. Sun, J. Bin Xu, C. P. Wong, Spherical core-shell Al@Al2O3 filled epoxy resin composites as high-performance thermal interface materials, Compos. Part A Appl. Sci. Manuf. 123 (2019) 260–269, https://doi.org/10.1016/j.compositesa.2019.05.024.

[27] Y. Huo, J. Wu, C.C. Lee, Solid solution softening and enhanced ductility in concentrated FCC silver solid solution alloys, Mater. Sci. Eng. A 729 (2018) 208–218, https://doi.org/10.1016/j.msea.2018.05.057.

[28] Q. Jia, G. Zou, W. Wang, H. Ren, H. Zhang, Z. Deng, B. Feng, L. Liu, Sintering mechanism of a supersaturated Ag-Cu nanoalloy film for power electronic packaging, ACS Appl. Mater. Interfaces 12 (2020) 16743–16752, https://doi.org/10.1021/acsami.9b20731.

[29] D. Kim, C. Chen, S. Noh, S.J. Lee, Z. Zhang, Y. Kimoto, T. Sugahara, K. Suganuma, Development of high-strength and superior thermal shock-resistant GaN/DBA die attach structure with Ag sinter joining by thick Ni metallization, Microelectron. Reliab. 100–101 (2019) 113380, https://doi.org/10.1016/j.microrel.2019.06.072.

[30] A. Jain, A.J.H. McGaughey, Thermal transport by phonons and electrons in aluminum, silver, and gold from first principles, Phys. Rev. B 93 (2016) 1–5, https://doi.org/10.1103/PhysRevB.93.081206.

[31] M.T. Lee, M.H. Fu, J.L. Wu, C.Y. Chung, S.J. Lin, Thermal properties of diamond/ag composites fabricated by eletroless silver plating, Diamond Relat. Mater. 20 (2011) 130–133, https://doi.org/10.1016/j.diamond.2010.11.017.

[32] T. McNutt, B. Passmore, J. Fraley, B. McPherson, R. Shaw, K. Olejniczak, A. Lostetter, High-performance, wide-bandgap power electronics, J. Electron. Mater. 43 (2014) 4552–4559, https://doi.org/10.1007/s11664-014-3376-y.

[33] K.W. Kim, A. Pashkin, H. Schäfer, M. Beyer, M. Porer, T. Wolf, C. Bernhard, J. Demsar, R. Huber, A. Leitenstorfer, Ultrafast transient generation of spin-density-wave order in the normal state of $BaFe_2As_2$ driven by coherent lattice vibrations, Nat. Mater. 11 (2012) 497–501, https://doi.org/10.1038/nmat3294.

[34] E. Çadirli, U. Böyük, H. Kaya, N. Maraşli, S. Aksöz, Y. Ocak, Dependence of electrical resistivity on temperature and Sn content in Pb-Sn solders, J Electron Mater 40 (2011) 195–200, https://doi.org/10.1007/s11664-010-1425-8.

[35] B. Hu, F. Yang, Y. Peng, C. Hang, H. Chen, C. Lee, S. Yang, M. Li, Effect of SiC reinforcement on the reliability of Ag nanoparticle paste for high-temperature applications, J. Mater. Sci. Mater. Electron. 30 (2019) 2413–2418, https://doi.org/10.1007/s10854-018-0514-y.

[36] S.R. Challa, A.T. Delariva, T.W. Hansen, S. Helveg, J. Sehested, P.L. Hansen, F. Garzon, A.K. Datye, Relating rates of catalyst sintering to the disappearance of individual nanoparticles during Ostwald ripening, J. Am. Chem. Soc. 133 (2011) 20672–20675, https://doi.org/10.1021/ja208324n.

[37] C. Oh, S. Nagao, K. Suganuma, Silver stress migration bonding driven by thermomechanical stress with various substrates, J. Mater. Sci. Mater. Electron. 26 (2015) 2525–2530, https://doi.org/10.1007/s10854-015-2717-9.

[38] Y. Chen, B. Li, X. Wang, X. Wang, Y. Yan, X. Li, Y. Wang, F. Qi, H. Li, Direct phase-change cooling of vapor chamber integrated with IGBT power electronic module for automotive application, IEEE Trans. Power Electron. 36 (2021) 5736–5747, https://doi.org/10.1109/TPEL.2020.3031372.

[39] X. Wang, Y. Mei, X. Li, M. Wang, Z. Cui, G.Q. Lu, Pressureless sintering of nanosilver paste as die attachment on substrates with ENIG finish for semiconductor applications, J. Alloys Compd. 777 (2019) 578–585, https://doi.org/10.1016/j.jallcom.2018.10.294.

[40] J. Acharya, J. Wilt, B. Liu, J. Wu, Probing the dielectric properties of ultrathin Al/Al2O3/Al Trilayers fabricated using in situ sputtering and atomic layer deposition, ACS Appl. Mater. Interfaces 10 (2018) 3112–3120, https://doi.org/10.1021/acsami.7b16506.

[41] A.M. Sadoun, I.M.R. Najjar, M.S. Abd-Elwahed, A. Meselhy, Experimental study on properties of Al–Al2O3 nanocomposite hybridized by graphene nanosheets, J. Mater. Res. Technol. 9 (2020) 14708–14717, https://doi.org/10.1016/j.jmrt.2020.10.011.

[42] F. Huo, C. Chen, Z. Zhang, Y. Wang, A. Suetake, K. Takeshita, Y. Yamaguchi, Y. Momose, K. Suganuma, Interface regulation of micro-sized sintered Ag-10Al composite based on in-situ surface modification and enhanced microstructure stability in power electronic packaging, Mater. Des. 240 (2024) 112863, https://doi.org/10.1016/j.matdes.2024.112863.

[43] A. van der Rest, H. Idrissi, F. Henry, A. Favache, D. Schryvers, J. Proost, J. P. Raskin, Q. Van Overmeere, T. Pardoen, Mechanical behavior of ultrathin sputter deposited porous amorphous Al2O3 films, Acta Mater. 125 (2017) 27–37, https://doi.org/10.1016/j.actamat.2016.11.037.

[44] K. Tazuddin, N.P. Biswas, Deciphering micro-mechanisms of plastic deformation in a novel single phase fcc-based MnFeCoNiCu high entropy alloy using crystallographic texture, Mater. Sci. Eng. A 657 (2016) 224–233, https://doi.org/10.1016/j.msea.2016.01.065.

[45] R. Pokharel, J. Lind, S.F. Li, P. Kenesei, R.A. Lebensohn, R.M. Suter, A.D. Rollett, In-situ observation of bulk 3D grain evolution during plastic deformation in polycrystalline Cu, Int. J. Plast. 67 (2015) 217–234, https://doi.org/10.1016/j.ijplas.2014.10.013.

[46] F. Mao, M. Taher, O. Kryshtal, A. Kruk, A. Czyrska-Filemonowicz, M. Ottosson, A. M. Andersson, U. Wiklund, U. Jansson, Combinatorial study of gradient Ag-Al thin films: microstructure, phase formation, mechanical and electrical properties, ACS Appl. Mater. Interfaces 8 (2016) 30635–30643, https://doi.org/10.1021/acsami.6b10659.

[47] S.Y. Wang, S.L. Wang, Y.R. Yang, X.D. Wang, D.J. Lee, High-temperature reactive wetting systems: role of lattice constant, Chem. Eng. Sci. 209 (2019) 115206, https://doi.org/10.1016/j.ces.2019.115206.

[48] B.C. Hornbuckle, T. Rojhirunsakool, M. Rajagopalan, T. Alam, G.P. Purja Pun, R. Banerjee, K.N. Solanki, Y. Mishin, L.J. Kecskes, K.A. Darling, Effect of Ta solute concentration on the microstructural evolution in immiscible Cu-Ta alloys, Jom 67 (2015) 2802–2809, https://doi.org/10.1007/s11837-015-1643-x.

[49] Y.F. Song, X.F. Ding, L.R. Xiao, X.J. Zhao, Z.Y. Cai, L. Guo, Y.W. Li, Z.Z. Zheng, Effects of two-stage aging on the dimensional stability of Al-Cu-Mg alloy, J. Alloys Compd. 701 (2017) 508–514, https://doi.org/10.1016/j.jallcom.2017.01.139.